Journal of Cleaner Production 434 (2024) 140089

Contents lists available at ScienceDirect

Journal of Cleaner Production

journal homepage: www.elsevier.com/locate/jclepro

Numerical investigation of a battery thermal management system integrated with vapor chamber and thermoelectric refrigeration

Ding Luo [a,b,**], Haifeng Wu [a], Jin Cao [a], Yuying Yan [c], Xuelin Yang [a], Bingyang Cao [b,*]

[a] College of Electrical Engineering & New Energy, China Three Gorges University, Yichang, China
[b] Key Laboratory for Thermal Science and Power Engineering of Ministry of Education, Department of Engineering Mechanics, Tsinghua University, Beijing, 100084, China
[c] Faculty of Engineering, University of Nottingham, University Park, Nottingham, UK

ARTICLE INFO

Handling Editor: Panos Seferlis

Keywords:
Battery thermal management system
Vapor chamber
Thermoelectric cooler
Numerical model
Maximum temperature

ABSTRACT

An efficient battery thermal management system is crucial for ensuring the working temperature environment of batteries and extending their lifespan. In this paper, a novel battery thermal management system combining vapor chambers and thermoelectric coolers is proposed to improve the battery's thermal behavior. Also, a complete fluid-thermal-electric multiphysics numerical model for the proposed system is built to predict its thermal performance under different cooling parameters. Results show that the use of thermoelectric coolers and vapor chambers can greatly lower the maximum temperature and temperature difference of batteries. Although the maximum temperature decreases with the increase of air convection heat transfer coefficient and coolant flow rate, the temperature difference increases at the same time. Under the given optimal air and water cooling parameters, it is noticed that as the input current of thermoelectric coolers increases, the maximum temperature and temperature difference show a pattern of decreasing first and then increasing. The optimal air convective heat transfer coefficient, coolant flow rate, and input current of 50 W/(m^2·K), 0.04 m/s, and 1.5 A, respectively, are suggested, which corresponds to the maximum temperature of 39.83°C and temperature difference of 5.97°C. The present research introduces a fresh perspective on efficient battery thermal management, offering detailed insights into the utilization of thermoelectric cooling for this purpose.

1. Introduction

Electric vehicles offer significant advantages in reducing greenhouse gas emissions and environmental pollution and witness rapid development in the context of increasingly serious environmental issues today. The application of lithium-ion batteries, characterized by their high energy density and extended lifespan, plays a pivotal role in the success of electric vehicles as they emerge as the primary option for energy storage (Osmani et al., 2023). However, the thermal behavior of lithium-ion batteries significantly affects their working performance. During high-rate charging and discharging, the batteries generate a substantial amount of heat. Insufficient dissipation of heat can cause it to accumulate within the battery pack, resulting in increased temperatures and temperature differences. Operating under extreme temperature differences or high temperatures can lead to performance degradation, accelerated battery aging, and even the occurrence of thermal runaway incidents (Shahid and Agelin-Chaab, 2022). Li-ion batteries have an acceptable temperature range for operation, which spans from 0°C to 60°C. However, the optimum range narrows down to 15°C–35°C (Verma et al., 2023). The research in (Lu et al., 2019) reveals that as long as the battery temperature falls between 20°C and 40°C, the impact of temperature on battery charging performance is negligible, but once the temperature exceeds this range, it has a pronounced effect on the battery performance. For example, the battery capacity will be decreased with the continuous charging and discharging process because of the increase in impedance. Additionally, the maximum temperature difference among batteries can not exceed 6°C to ensure a good performance of Li-ion batterie (Isfahani et al., 2023). Hence, a reliable battery thermal management system (BTMS) is essential to maintain the battery within the suitable temperature range at all times (Liu and Zhang, 2020).

The BTMS is usually divided into several main types: air-based BTMS

* Corresponding author.
** Corresponding author.
E-mail addresses: Ding_L@outlook.com (D. Luo), 202208110021013@ctgu.edu.cn (H. Wu), caojin@ctgu.edu.cn (J. Cao), Yuying.Yan@nottingham.ac.uk (Y. Yan), xlyang@ctgu.edu.cn (X. Yang), caoby@tsinghua.edu.cn (B. Cao).

https://doi.org/10.1016/j.jclepro.2023.140089
Received 1 September 2023; Received in revised form 27 November 2023; Accepted 4 December 2023
Available online 8 December 2023

Nomenclature

Symbols

A	area, m^2
C	specific heat, J/(kg·K)
$\vec{E}$	electric field density vector, V/m^2
h	heat transfer coefficient, $W/(m^2 \cdot K)$
I	current, A
$\vec{J}$	current density vector, A/m^2
k	thermal conductivity, W/(m·K)
P	pressure, Pa
P_{in}	input power, W
q_+	heat of the positive pole, W/m^3
q_-	heat of the negative pole, W/m^3
Q	heat production power, W
Q_b	volume heat generation rate, W/m^3
Q_c	heat absorption of the cold side, W
Q_h	heat release of the heat side, W
$\dot{Q}_m$	source term
R	resistance, Ω
R_j	ohmic internal resistance, Ω
R_{po}	polarization internal resistance, Ω
T	temperature, K
V	volume, m^3
$\vec{v}$	velocity vector

Greek symbols

α	seebeck coefficient, μV/K
ρ	density, kg/m^3
λ	thermal conduction, W/K
μ	dynamic viscosity, Pa·s
σ	electrical conductivity, S/m
φ	electrical potential, V

Subscripts

b	battery
c	cold side
co	copper electrodes
h	hot side
L	length
m	material
n	n-type legs
p	p-type legs
w	water

Abbreviations

BTMS	battery thermal management systems
CFD	computational fluid dynamics
COP	coefficient of performance
HP	heat pipe
LC	liquid cooling
LFP	lithium iron phosphate
MHPA	micro heat pipe array
PCM	phase change material
TEC	thermoelectric cooler
VC	vapor chamber

(Abdulrasool Hasan et al., 2023), liquid-based BTMS (Liang et al., 2022), heat pipe (HP)-based BTMS (Jouhara et al., 2021), phase change material (PCM)-based BTMS (Wazeer et al., 2022), and the combination of the above two or more cooling methods (Abbas et al., 2021). Typically, air cooling is the favored cooling technique owing to its uncomplicated design and cost-effectiveness. Nevertheless, the cooling effectiveness of air cooling is limited by the low thermal conductivity and low specific heat capacity of air (Sharma and Prabhakar, 2021). In comparison to traditional air cooling, liquid cooling can deliver higher cooling power and significantly reduce the battery temperature, yet it poses a risk of leakage and does not deliver satisfactory temperature uniformity (Deng et al., 2018). PCM cooling technology is currently known as one of the most efficient methods. Unlike active approaches such as active air cooling or liquid cooling, it harnesses the latent heat released during the phase change process of PCM materials to provide sufficient cooling energy to the battery while ensuring a high temperature uniformity (Heyhat et al., 2020). However, the PCM cooling method delivers the disadvantage of low thermal conductivity, which restricts its extensive commercial usage (Murali et al., 2021).

Thanks to the ultrahigh thermal conductivity, heat pipes, based on the principle of liquid-gas phase transition, are regarded as a promising alternative cooling method (Weragoda et al., 2023). Zheng et al. (2023) proposed a BTMS combined with air cooling and heat pipes to regulate the battery temperature, and utilized computational fluid dynamics (CFD) tools to study its thermal performance; Based on the simulation results, it can be observed that the temperature difference among batteries is directly proportional to the discharge rate, while adjusting the air temperature and flow speed merely helps to mitigate the temperature increase. Jang et al. (2022) designed three BTMS, namely, liquid cooling (LC), A-type heat pipe liquid cooling (LCA), and B-type heat pipe liquid cooling (LCB), and compared their thermal performance through CFD simulations; the results show that the maximum temperature of batteries in LCB is 6.1°C and 9.4°C lower than that of LC under basic and optimized conditions, respectively. It can be seen that introducing heat pipes into traditional air-based and liquid-based BTMS can effectively improve their thermal performance. Ren et al. (2021) developed a new type of active air-cooled BTMS based on the U-shaped micro heat pipe array (MHPA) to reduce the temperature rise and improve the temperature uniformity of the battery during the entire charge and discharge process; Their results show that temperature differences of the active air cooling with U-shaped MHPA, passive air cooling with U-shaped MHPA, and passive air cooling without U-shaped MHPA are 2.53°C, 2.27°C, and 3.75°C, respectively. The given literature proves that the use of heat pipes is an effective manner to improve the temperature uniformity of the BTMS.

Thermoelectric cooling, as another promising thermal management technology, has aroused widespread interest among researchers in recent years. When an electric current flows through a thermoelectric cooler (TEC), the Peltier effect results in heat being released from the hot side and absorbed by the cold side, and the magnitude of the heat generated is directly proportional to the input current. Based on this principle, the TEC can be used to regulate the temperature of battery packs, including heating and cooling, and has the advantages of fast response speed, small size, easy control, and no refrigerant pollution (Lyu et al., 2019). Jiang et al. (2019) designed a hybrid BTMS combining TECs and PCMs and analyzed its performance via experiments; the results indicate that the TEC is proficient in reducing battery temperature and significantly extending the operational duration. Liao et al. (2021) designed an active-passive hybrid full-temperature BTMS that combines TECs and PCMs, and investigated its thermal performance through CFD simulations; The findings reveal that even under a high discharge rate of 3C, the system can maintain the maximum temperature of batteries below 45°C, while ensuring that the maximum temperature difference during the discharge process remains within 3°C. Additionally, when comparing it to PCM cooling alone, the integration of TECs and PCMs results in a reduction of approximately 10°C in the maximum battery

temperature. This significant improvement highlights the promising application potential of TECs in battery thermal management. Liu et al. (2022) proposed a BTMS that combines TECs and PCMs, and introduced fins to improve its thermal performance; They found that when the fin height is increased from 2 mm to 8 mm, the temperature control time is extended by 12%, while the temperature difference is increased by 13.7%. Nonetheless, the current investigation into the performance of thermoelectric-based BTMS primarily relies on CFD simulations or rudimentary analysis. There is a lack of precise and systematic performance analysis for thermoelectric-based BTMS in current studies.

Researchers have conducted extensive research on the BTMS that combine PCMs and TECs. However, when the battery operates under high discharge rates, the temperature uniformity of the battery is significantly reduced due to the increased heat release. To address this issue, this work tries to make full use of the advantages of both heat pipes and TECs. It introduces a novel BTMS that combines TECs with vapor chambers (VCs, a flat heat pipe), to improve battery thermal performance. This BTMS implements air cooling at the top and water cooling at the bottom for efficient heat dissipation. Besides, a complete fluid-thermal-electric multiphysics numerical model is established to systematically evaluate the thermal behavior of the BTMS. To highlight the effectiveness of TECs and VCs, three different configurations are developed and compared: the BTMS with VCs and TECs (BTMS-VC&TEC), the BTMS without TECs (BTMS-VC), and the BTMS without VCs (BTMS-TEC). Finally, the effects of coolant flow rate, TEC input current, and air heat transfer coefficient on the maximum temperature and temperature uniformity of the battery pack are studied.

2. Model development

This paper investigates the thermal performance of the BTMS, with the battery pack comprising three square LFP (Lithium iron phosphate) batteries as the objective of the study. The BTMS employs a combination of TEC, VC, air cooling, and water cooling to achieve efficient temperature regulation. The simulation analysis is carried out using the commercial software of COMSOL Multiphysics.

2.1. Three-dimensional geometric model of the BTMS

The BTMS consists of three battery cells, four VCs, four thermoelectric coolers (TECs), one finned heat sink, and one liquid cooling plate, where the VC features a U shape (Ren et al., 2021) and is divided into two types: long VC and short VC, as shown in Fig. 1. The battery cell (Liu et al., 2022) with a capacity of 50 A·h is adopted, which features a size of 90 mm × 70 mm × 27 mm. To effectively dissipate heat generated by batteries, three battery cells are all wrapped by VCs, where the first battery cell on the left hand in the figure is wrapped by two short VCs, and the second (or third) battery cell is wrapped by one long VC. The height and width of both VCs are 76 mm and 90 mm, while the lengths for the long VC and short VC are 30 mm and 16.5 mm, respectively. Here, the VC, as a super thermal conductor, consists of two sections: evaporator and condenser. The heat generated by the battery is conveyed to the VC, leading to the evaporation of the internal working fluid. Subsequently, the gaseous working fluid flows to the low-temperature region within the VC, undergoing a phase transition back to the liquid state. This gas-liquid phase transition process enables the VC to achieve efficient heat transfer. In this design, the central portion of the VC, absorbing heat from the battery, can be treated as an evaporator chamber, while heat dissipation occurs at both ends, resembling condensers. To facilitate numerical calculations, VCs are simplified as homogeneous solid blocks with uniform thermophysical properties and ultrahigh thermal conductivity (Greco et al., 2014). On the bottom side of VCs, a liquid cooling plate with a size of 93 mm × 90 mm × 5 mm is equipped, and a U-shaped water channel with a diameter of 4 mm is designed inside the cooling plate to improve the liquid cooling performance. To utilize the advantages of precise temperature

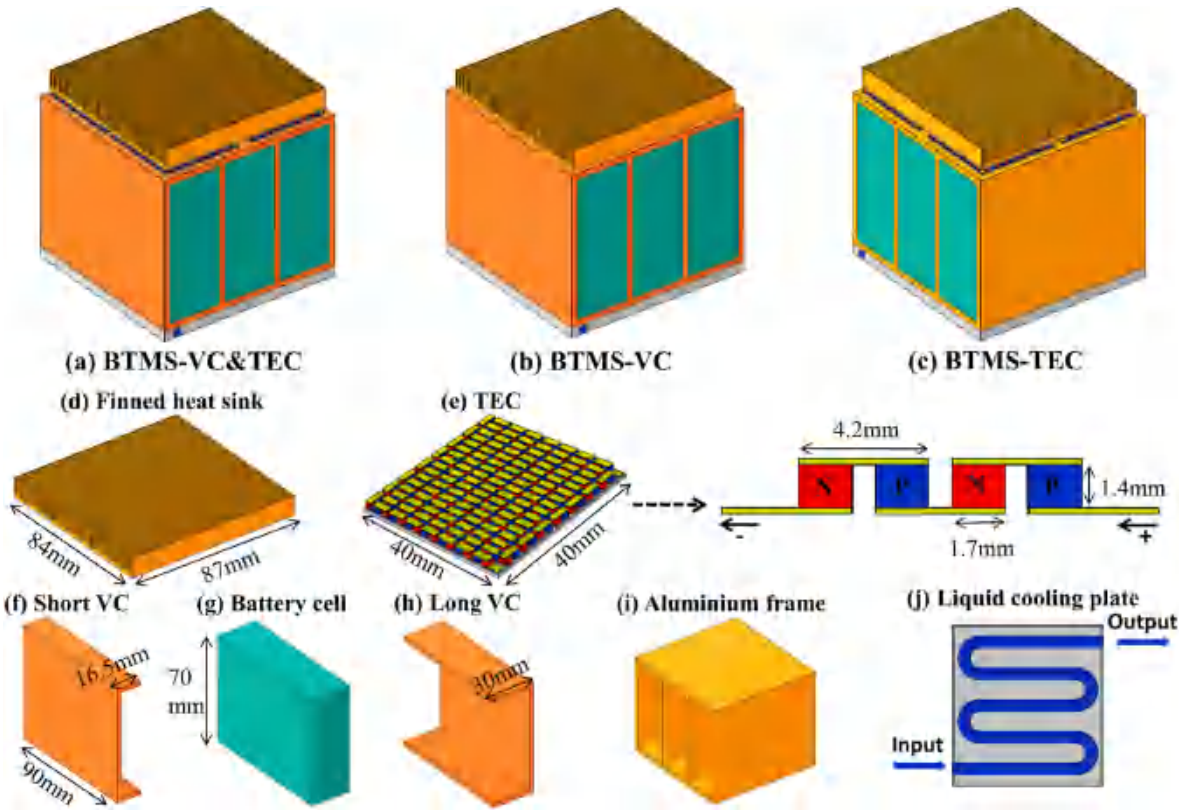

Fig. 1. Structure of the BTMS. (a) BTMS-VC&TEC; (b) BTMS-VC; (c) BTMS-TEC; (d) Finned heat sink; (e) TEC; (f) Short VC; (g) Battery cell; (h) Long VC; (i) Aluminium frame; (j) Liquid cooling plate.

Table 1
Properties of different materials.

Property	Aluminum	Battery (Liu et al., 2022)	VC (Chen et al., 2021)
Density (kg/m^3)	2700	1838.2	8978
Specific heat capacity (J/(kg·K))	900	1150	381
Thermal conductivity (W/(m·K))	238	15.3, 15.3, 0.9 (kx, ky, kz)	2000

control and fast response in thermoelectric refrigeration, four TECs are employed on the top side of VCs. The TEC is comprised of 127 pairs of p- and n-type thermoelectric legs, 256 copper electrodes, and two ceramic plates. When an electric current passes through the TEC, the bottom and top ends of the TEC will absorb and release heat respectively, due to the Peltier effect. However, the heat accumulation on the hot end of the TEC will deteriorate its cooling performance. Consequently, a finned heat sink is attached to the hot end of TECs to dissipate heat. The overall size of the heat sink is 87 mm × 84 mm × 10 mm, and the fin thickness and spacing are both 1 mm.

Considering the high cost of nanosynthesised thermoelectrics, the TECs made by commercial synthesis methods are used, and they are exclusively utilized on the upper part of the VC, with no implementation on the lower part. Additionally, thanks to the use of TECs, the cooling demands of the BTMS can be satisfied through air cooling, allowing for the adoption of a finned heat sink at the top, eliminating the necessity for a liquid cooling plate. To demonstrate the effectiveness of the TECs and VCs on battery thermal management, the given BTMS with both VCs and TECs (as shown as BTMS-VC&TEC in Fig. 1(a)) is compared to the other two configurations: the BTMS without TECs (as shown as BTMS-VC in Fig. 1(b)), and the BTMS without VCs (as shown as BTMS-TEC in Fig. 1(c)). In the BTMS-VC, the finned heat sink is directly contacted with VCs, while in the BTMS-TEC, the VCs are replaced by an aluminum frame with a size of 93 mm × 90 mm × 76 mm. Table 1 lists the material properties of different components (exclude TEC) used in the BTMS, where the properties of batteries and VCs refer to (Liu et al., 2022; Chen et al., 2021), respectively. The finned heat sink and liquid cooling plate are made of aluminum materials, due to their high thermal conductivity and low weight. Detailed parameters of the TEC are listed in Table 2, where the thermoelectric legs are made of Bi_2Te_3-based materials, and the corresponding material properties are derived from the previous work (Hu et al., 2023).

2.2. Governing equations of the fluid-thermal-electric multiphysics numerical model

In this part, the principles of the multiphysics numerical model are introduced in detail. Here, the battery thermal model adopts the theoretical calculation model of heat generation rate proposed by (Mali et al., 2021), which is:

$$Q_b = \frac{I_b}{V}\left[(E_0 - U) + T_b\frac{dE_0}{dT_b}\right] = \frac{1}{V}\left[I_b^2(R_j + R_{po}) + I_b T_b\frac{dE_0}{dT_b}\right] \quad (1)$$

where Q_b and V represent the volume heat generation rate of the battery and the volume of the battery; E_0 and U represent the open-circuit voltage and operating voltage of the battery respectively; R_j and R_{po} represent the ohmic internal resistance and polarization internal resistance of the battery respectively; I represents the working current, and T_b represents the temperature of the battery.

The electrochemical reaction heat $\frac{I_b T_b dE_0}{dT_b}$ is too small and usually ignored. Thus, Eq. (1) can be simplified as:

$$Q_b = \frac{I_b}{V}(E_0 - U) = \frac{I^2 R}{V} \quad (2)$$

In addition, the poles will also generate heat when the battery is working. To improve the calculation efficiency, it is necessary to simplify the battery model by eliminating some small parts such as poles and screws. Therefore, the heat generated by the poles is assumed to be concentrated on the main body of the battery, and Eq. (2) is written by:

$$Q_b = \frac{Q_{core}V_{core} + q_+V_+ + q_-V_-}{V} \quad (3)$$

here Q_{core} and V_{core} represent the volume heat generation rate and the volume of the main battery body. According to Eq. (3), the total heat generation of LFP batteries under different discharge rates can be calculated using the battery parameters in (Liu et al., 2022), as listed in Table 3. The proposed BTMS can meet the heat dissipation requirements under extremely high discharge rate conditions. To highlight its advantages, the discharge rate of 5C is used in this paper. Additionally, the battery is simplified as homogeneous solid blocks with uniform thermophysical properties.

For the flow domain, the flow pattern used in this paper is laminar flow, and the water flow in the liquid cooling plate is regarded as incompressible. The conservation equations for the energy, mass, and momentum in the flow domain can be expressed as (Yue et al., 2022):

$$\nabla\cdot(\rho_w C_w \vec{v} T_w) - \nabla\cdot(k_w \nabla T_w) = 0 \quad (4)$$

$$\nabla\cdot\vec{v} = 0 \quad (5)$$

$$\rho_w \nabla\cdot(\vec{v}\vec{v}) = \nabla p + \nabla\cdot(\mu\nabla\vec{v}) \quad (6)$$

where ρ_w, C_w, and k_w are the density, specific heat, and thermal conductivity of water respectively; T_w is the temperature of water, and $\vec{v}$ is the velocity vector; μ and p are the dynamic viscosity and pressure respectively.

For the solid domain, the governing equation can be expressed by the energy conservation (Luo et al., 2023b):

$$\nabla\cdot(k_m\nabla T) + \dot{Q}_m = 0 \quad (7)$$

where k_m and $\dot{Q}_m$ are respectively the thermal conductivity and energy source term of different materials. In different computational domains, the energy source can be expressed as (Meng et al., 2021):

Table 3
Total heat generation of the battery under different discharge rates.

Discharge rate (C)	Heat production power (W)
1C	7.48
3C	16.82
5C	29.90

Table 2
Datasheet of the TEC (Hu et al., 2023).

	Seebeck coefficient (μV/K)	Thermal conductivity (W/(m·K))	Electrical resistivity (10^{-5} Ω·m)	Size (L × W × H mm^3)
p-type legs	$-1.593\times10^{-9}T^2+1.364\times10^{-6}T-7.062\times10^{-5}$	$1.071\times10^{-5}T^2-8.295\times10^{-3}T+2.625$	$1.311T^2-1.364\times10^{3}T+4.023\times10^{5}$	1.7 × 1.7 × 1.4
n-type legs	$7.393\times10^{-11}T^2-2.500\times10^{-7}T-8.494\times10^{-5}$	$1.870\times10^{-5}T^2-1.447\times10^{-2}T+3.680$	$0.657T^2-7.136\times10^{2}T+2.463\times10^{5}$	1.7 × 1.7 × 1.4
copper electrodes	–	400	1.67×10^{-3}	4.2 × 1.7 × 0.2
ceramic plates	–	22	–	40 × 40 × 0.8

$$\dot{Q}_m=\begin{cases} Q_b; \text{batteries} \\ \sigma_p^{-1}\vec{J}^2-\nabla\alpha_p(T)\vec{J}T_p-\dfrac{\partial\alpha_p(T)}{\partial T_p}T_p\vec{J}\cdot\nabla T; \text{p}-\text{type thermoelectric legs} \\ \sigma_n^{-1}\vec{J}^2-\nabla\alpha_n(T)\vec{J}T_n-\dfrac{\partial\alpha_n(T)}{\partial T_n}T_n\vec{J}\cdot\nabla T; \text{n}-\text{type thermoelectric legs} \\ \sigma_{co}^{-1}\vec{J}^2; \text{copper electrodes} \\ 0; \text{VC, heat sink, cooling plate, and ceramic plates} \end{cases} \tag{8}$$

where p, n, and co represent p-type thermoelectric legs, n-type thermoelectric legs, and copper electrodes, respectively. σ^{-1} and α are the electrical resistivity and Seebeck coefficient respectively. $\vec{J}$ is the current density vector.

Furthermore, the computational domain, which encompasses current flow and includes copper electrodes, p-type and n-type thermoelectric legs, adheres to the governing equations of the electric field, as follows (Luo et al., 2023a):

$$\vec{E}=-\nabla\varphi+\alpha_{p,n}(T)\nabla T \tag{9}$$

$$\vec{J}=\sigma_m\vec{E} \tag{10}$$

$$\nabla\cdot\vec{J}=0 \tag{11}$$

where φ and $\vec{E}$ are the electrical potential and electrical field density vector respectively.

2.3. Boundary conditions

In this study, the finite element method (FEM) is employed to compute the aforementioned equations. Moreover, it is necessary to establish the required boundary conditions for conducting the finite element simulation. For the air cooling, its heat transfer between the finned heat sink and air can be defined as:

$$-k\frac{\partial T}{\partial n}=h_{air}(T_{air}-T) \tag{12}$$

where h_{air} and T_{air} are respectively the heat transfer coefficient and temperature of the air. For the air cooling-based BTMS, the heat transfer coefficient usually falls in the range of 10–100 W/(m^2·K) (Hamisi et al., 2022). Therefore, h_{air} is set to vary from 10 to 100 W/(m^2·K) at every 10 W/(m^2·K) in this study to analyze the impact of air cooling on the BTMS performance. Besides, T_{air} is fixed at 20°C herein.

Regarding the water cooling, a velocity inlet boundary condition is specified on the inlet surface of the liquid cooling plate, with the water temperature being set as 20°C. The water flow rate is set to vary from 0.01 to 0.1 m/s at every 0.01 m/s, to analyze the influence of water cooling. Considering that the maximum coolant flow speed is lower than 0.1 m/s and the calculated Reynolds number is lower than 2000, the simulations in this work adopt the laminar model (Yi et al., 2022). In addition, the finite element method is applied to solve the above discretized governing equations; The relative tolerance is set as 0.001; And the SIMPLE algorithm is used for the fluid flow.

Additionally, the current input boundary condition is specified on one terminal of each TEC, while the other terminal is grounded. With the given settings, the TEC can produce cooling power for VCs, thus reducing the battery temperature.

2.4. Parameter definitions

The cooling performance of the TEC substantially influences the heat dissipation of batteries, which can be characterized by the cooling power (Q_c) and coefficient of performance (COP). According to the literature (Zhao and Tan, 2014), the equations for the cooling power and heating power of a TEC are defined as:

$$Q_c=\alpha I_{TEC}T_c-\frac{1}{2}I_{TEC}^2R_{TEC}-\lambda_{TEC}(T_h-T_c) \tag{13}$$

$$Q_h=\alpha I_{TEC}T_h+\frac{1}{2}I_{TEC}^2R_{TEC}-\lambda_{TEC}(T_h-T_c) \tag{14}$$

where, T_c and T_h are respectively temperatures on the cold and hot ends of the TEC; I_{TEC}, R_{TEC}, and λ_{TEC} are respectively the input current, resistance, and thermal conduction of the TEC.

Therefore, the TEC input power can be obtained by combining Eqs (13) and (14), which is:

$$P_{in}=Q_h-Q_c=I_{TEC}^2R_{TEC}+\alpha I_{TEC}(T_h-T_c) \tag{15}$$

Finally, the expression for COP can be obtained：

$$\text{COP}=\frac{Q_c}{P_{in}} \tag{16}$$

Q_c and COP are used to assess the cooling performance of the TEC. As for the overall thermal performance of the BTMS, it can be characterized by the maximum temperature (T_{max}) and maximum temperature difference (ΔT_{max}) of batteries. The mentioned parameters used to calculate the Q_c, COP, T_{max} and ΔT_{max} are extracted from FEM simulation results.

2.5. Grid independence analysis

The verification of grid cell independence is vital for ensuring accurate calculation results. In this study, the mesh was generated using COMSOL Multiphysics, as shown in Fig. 2. The maximum temperature and temperature difference of the batteries are obtained using five different grid systems with grid numbers of 346711, 528395, 893537, 1548240, and 3767719, as presented in Table 4. It is evident that the aforementioned two parameters remain relatively stable when the grid number exceeds 1548240. Therefore, the grid density corresponding to 1548240 grids is selected for grid generation and subsequent simulations.

2.6. Model verification

The proposed prototype of the BTMS is currently being manufactured, but it will take plenty of time. For this reason, the experimental data in the previously published work is used to perform model verification herein. The structure of the BTMS that combines TECs and VCs in (Ren et al., 2021) is built and numerically simulated using the developed steady-state fluid-thermal-electric multiphysics model. Fig. 3 shows the comparison of the maximum temperature difference between experimental data in (Ren et al., 2021) and simulation results in this work. It can be found that the simulation results are in good agreement with the experimental results with a maximum error of about 7%, which supports the reliability and validity of the subsequent simulation results to a certain extent.

3. Results and discussion

In this section, a comprehensive study is conducted to explore the thermal behavior of the BTMS, taking into consideration various parameters including air convective heat transfer coefficient, coolant flow rate, TEC input current, and VC thermal conductivity. The allowable battery temperature and maximum temperature difference for the BTMS are set below 40°C and 6°C (Isfahani et al., 2023) respectively.

3.1. Exploration of the working range of the TEC input current

According to Eq. (11), if the TEC input current surpasses a certain

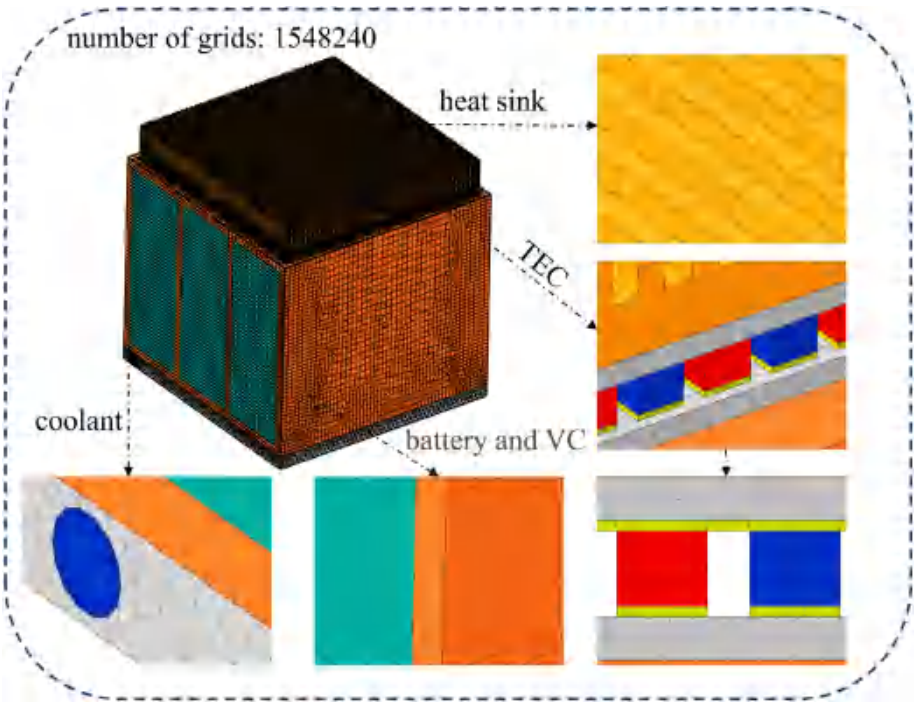

Fig. 2. Grid distribution of the BTMS when the grid number is 1548240.

Table 4
Maximum temperature and temperature difference under different grid numbers.

Grid numbers	Maximum temperature (°C)	Temperature difference (°C)
346711	42.19	6.61
528395	41.01	6.04
893537	40.41	5.98
1548240	39.83	5.97
3767719	39.76	5.96

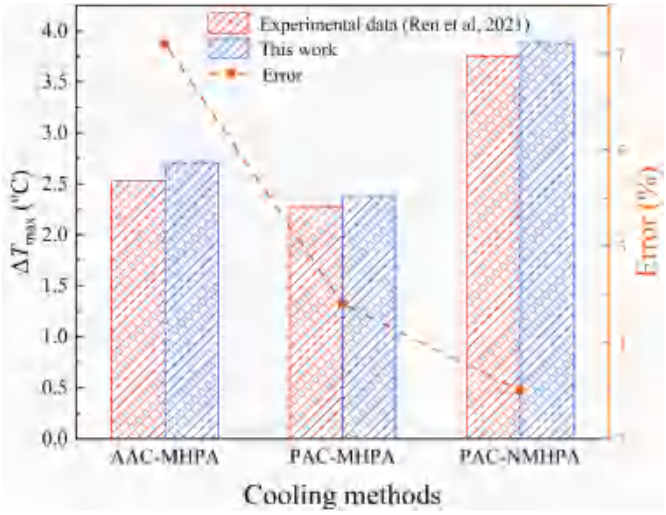

Fig. 3. Comparison of the maximum temperature difference between numerical results and experimental results. (Note: AAC for active air cooling, PAC for passive air cooling, MHPA for micro heat pipe array, and NMHPA for none MHPA).

threshold, the Joule heat generated could exceed the Peltier heat, leading to a negative value. In such a scenario, the TEC ceases to function as a cooler and instead becomes a heater. As a result, it is essential to determine a suitable range of the TEC input current as a prerequisite for analyzing the thermal performance of the BTMS. Here, we carried out a thermal-electric numerical analysis for only TECs. During the numerical simulation of the TEC, the temperature on the lower side of TECs is fixed at 27°C, while the temperature on the upper side is set to vary within the range of 27°C–47°C to investigate the influence of temperature difference on the cooling performance of the TEC.

Fig. 4 shows the temperature and potential distribution of a single TEC at the input current of 1.5 A and temperature difference of 10°C. Due to the relatively higher thermal resistance, the temperature gradient primarily occurs within the thermoelectric legs, as shown in Fig. 4(a). The input current prompts the carriers (electrons in n-type legs and holes in p-type legs) to migrate from the lower side to the upper side, causing heat absorption on the lower side and heat dissipation on the upper side. Meanwhile, the temperature difference from the upper side to the lower side propels the carriers in the opposite direction. Consequently, the temperature difference on both sides of the TEC deteriorates its cooling performance. In situations with a significant temperature difference, it becomes necessary to increase the input current of the TEC to overcome the resistance caused by the temperature difference and enhance the cooling performance. The electric potential gradually increases from the grounded surface to the current input surface, and at an input current of 1.5 A, the maximum potential is 2.42 V, as shown in Fig. 4(b). The calculated power by multiplying the input current by the potential, that is 3.63 W, which is slightly lower than the TEC input power calculated by Eq. (13), because the input power also needs to overcome the resistance caused by temperature difference. Besides, Q_c and COP can be computed by extracting the corresponding data from simulation results.

Fig. 5 plots the functions of TEC cooling power Q_c and COP as input current at different temperature differences. The cooling power of the TEC gradually amplifies as the current increases, but as the current

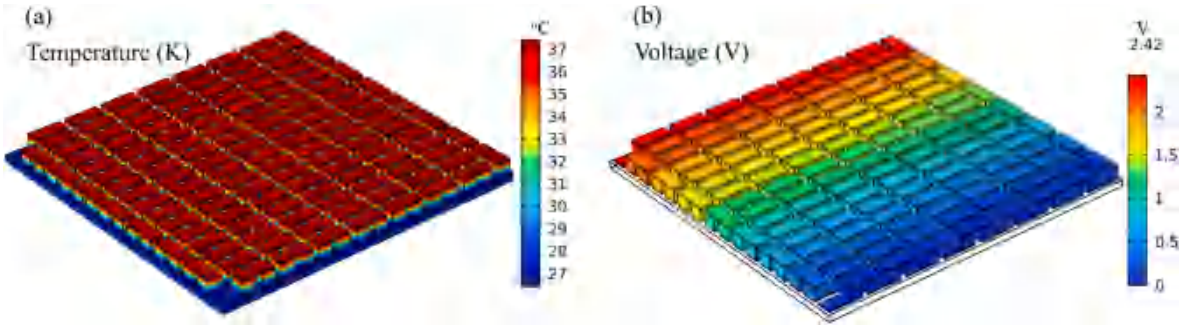

Fig. 4. Numerical results of the TEC at the input current of 1.5 A and temperature difference of 10°C. (a) Temperature distribution of the TEC; (b) Voltage distribution of the TEC.

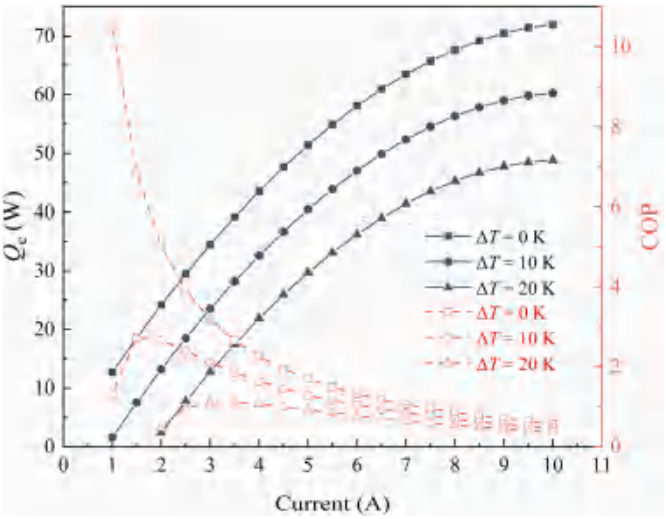

Fig. 5. Functions of TEC cooling power Q_c and COP as input current at different temperature differences.

becomes sufficiently high, the rate of increase in cooling power becomes slower. Furthermore, the cooling power diminishes as the temperature difference increases. As for the COP, when the temperature difference is 0°C, the COP continuously decreases with an increase in TEC input current. However, in practical situations where there exists a temperature difference between the two ends of the TEC, the COP exhibits a parabolic relationship with the input current, and the peak value of COP decreases with an increase in temperature difference. To make a tradeoff between Q_c and COP, it is recommended that the input current of TEC shall not exceed approximately 6 A.

Furthermore, numerical simulations for the BTMS thermal performance under different TEC input currents are carried out to analyze the influence of current, as shown in Fig. 6. Here, the air convective heat transfer coefficient and coolant flow rate are set as 50 W/(m^2·K) and 0.04 m/s respectively. It is evident that as the input current increases, the temperature of the finned heat exchanger rises, primarily caused by the augmented Peltier heat on the hot side of the TEC. Simultaneously, the TEC produces higher cooling power on the cold side, resulting in a decrease in battery temperature. Nevertheless, once the current surpasses 2.5 A, the battery temperature begins to rise along with the increasing current, eventually exceeding 40°C at 3 A. This is mainly attributed to the deteriorated cooling performance caused by the temperature difference across the TEC. Therefore, the use of excessively high TEC input currents is not advisable as it leads to excessive energy consumption and adversely affects the temperature performance of the battery.

Fig. 7 shows the detailed temperature distributions of batteries under different TEC input currents. When the current ranges from 1.5 A to 2.5 A, the battery temperature exhibits similar performance and all within the allowable value. Considering the smaller energy consumption, it is preferred to choose an input current of 1.5 A, corresponding to the maximum temperature and temperature difference of 39.83°C and 5.97°C respectively. With further increases in current, both the maximum temperature and temperature difference of the batteries increase, reaching 48.75°C and 6.7°C respectively when the current is 5 A. Furthermore, at a current of 5 A, the temperature at the upper end of the battery is already higher than that at the lower end. This is primarily due to the large amount of heat generated on the hot side of the TECs in this situation, and the finned heat sink's inability to effectively dissipate the heat. As a result, the high temperature difference across both ends of the TEC impairs its cooling performance, leading to lower cooling performance compared to the liquid cooling plate.

3.2. Comparison of the BTMS thermal performance between three configurations

In this section, the BTMS-VC&TEC is compared with the BTMS-VC and BTMS-TEC to demonstrate the effectiveness of TECs and VCs in improving thermal performance. Fig. 8 shows the effect of the coolant flow rate on the BTMS thermal performance under three configurations. Here, the convective heat transfer coefficient and TEC input current are set as 50 W/(m^2·K) and 1.5 A respectively. The maximum temperature shows a decrease as the coolant flow rate increases, specifically for the BTMS-VC&TEC and BTMS-TEC (as depicted in Fig. 8(a)), as the water cooling performance is improved with an increase in flow rate, and the use of TECs can amplify the air cooling performance of the finned heat sink. However, the situation for the temperature difference is quite different. As the increase of coolant flow rate, the temperature difference in the three configurations decreases first and then increases, and the temperature difference of the BTMS-TEC is greatly larger than that of the other two configurations, as shown in Fig. 8(b). This is due to the fact that the temperature on the bottom side of batteries decreases with a higher flow rate, while the fixed convective heat transfer coefficient maintains a relatively constant and high temperature on the top side of batteries. Additionally, for the BTMS with TECs, when the coolant flow rate is below 0.03 m/s, the air cooling on the top side is superior to the water cooling on the bottom side, resulting in a larger temperature difference. However, with an increase in flow rate, the water cooling performance gradually improves and surpasses the air cooling performance, and the battery heat of the BTMS-TEC can not be effectively transferred to the cooling devices due to the absence of VCs, leading to a corresponding trend in temperature difference in Fig. 8(b).

Fig. 9 shows the effect of air convective heat transfer coefficient on the thermal performance under three configurations. Here, the coolant flow rate and TEC input current are set as 0.04 m/s and 1.5 A respectively. With the increase of heat transfer coefficient, the maximum temperature of all three configurations decreases (as shown in Fig. 9(a)),

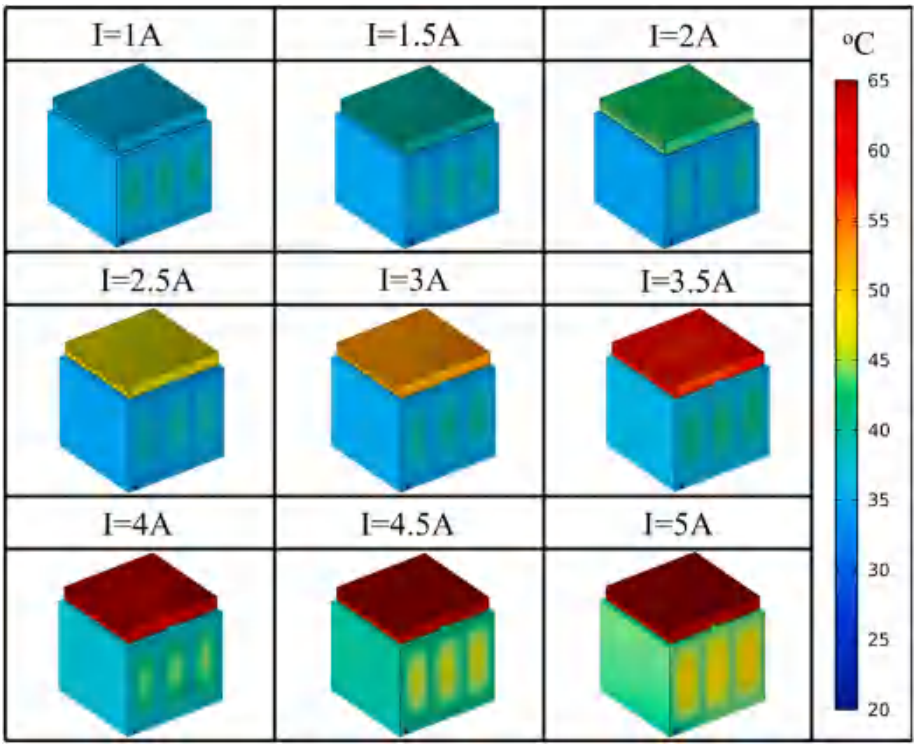

Fig. 6. Temperature distributions of the BTMS under different TEC input currents.

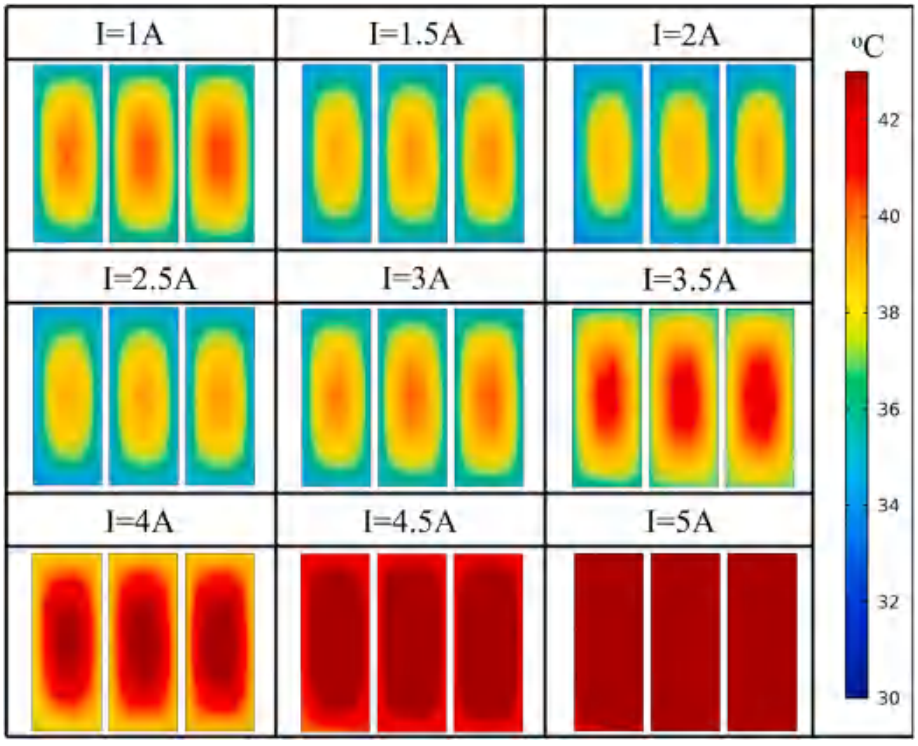

Fig. 7. Temperature distributions of the battery pack under different TEC input currents.

and the temperature difference decreases first and then increases (as shown in Fig. 9(b)). It is obvious that the use of TECs can greatly lower the maximum temperature, because the TEC amplifies the cooling performance of the air cooling. The decrease in temperature difference is due to the improvement of air cooling performance and the reduction of difference in cooling performance between the TEC and air cooling at the upper end of the battery and the water cooling at the lower end of the battery. However, as the heat transfer coefficient further increases, the difference in cooling performance between them increases, leading to an increase in temperature difference. Similarly, the temperature difference of the BTMS-TEC is much larger than that of the other two configurations, due to the absence of VCs. Considering the thermal performance and energy consumption of the system, a heat transfer coefficient of about 50 W/(m^2·K) is suggested, because a temperature

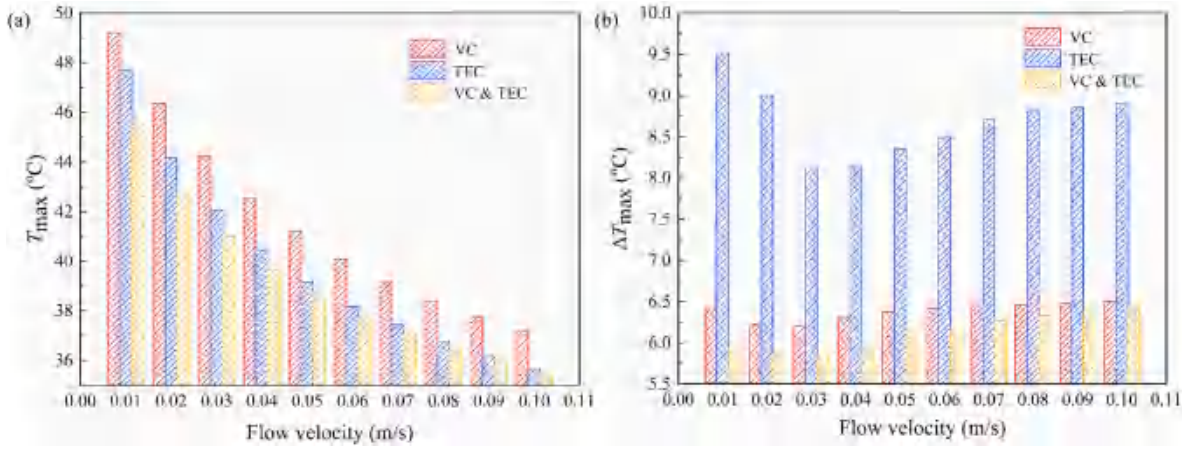

Fig. 8. Effect of coolant flow rate on the BTMS thermal performance under three configurations. (a) T_{max}; (b) ΔT_{max}.

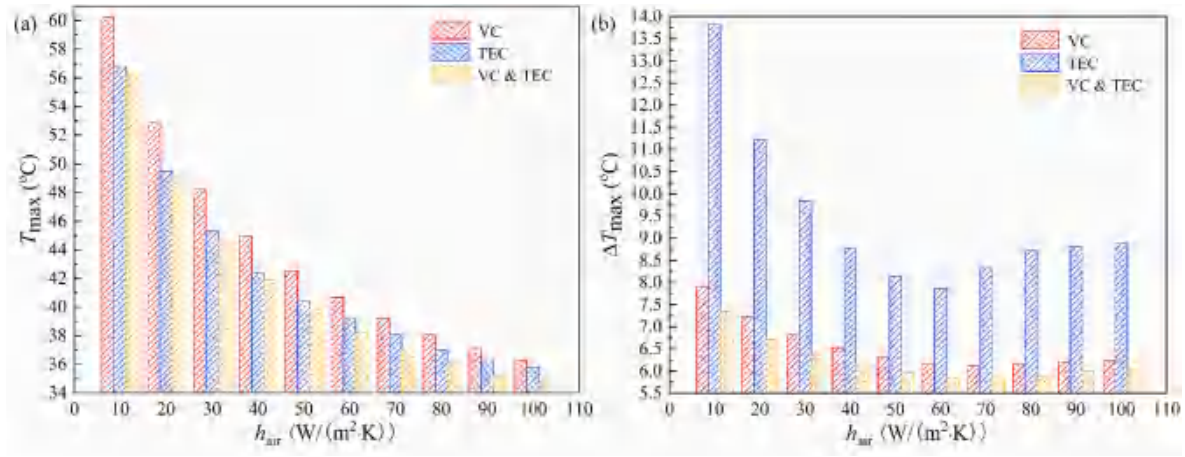

Fig. 9. Effect of air convective heat transfer coefficient on the BTMS thermal performance under three configurations. (a) T_{max}; (b) ΔT_{max}.

difference below 6°C already meets the battery temperature requirements (Isfahani et al., 2023), and if the heat transfer coefficient is greater than 50 W/(m^2·K), the energy consumption for air cooling will be significant (Jiang and Qu, 2019).

Combined with Figs. 8 and 9, it can be concluded that the TEC can greatly reduce the maximum temperature of the battery, and the VC can greatly improve the temperature uniformity. The combination of the TEC and VC enables the battery to achieve ultrahigh thermal performance, and the impact of various cooling parameters on the BTMS is comprehensively analyzed in the following sections.

3.3. Coupling influences of air convective heat transfer coefficient and coolant flow rate

Fig. 10 shows the effect of air convective heat transfer coefficient on the BTMS thermal performance under different coolant flow rates. Here,

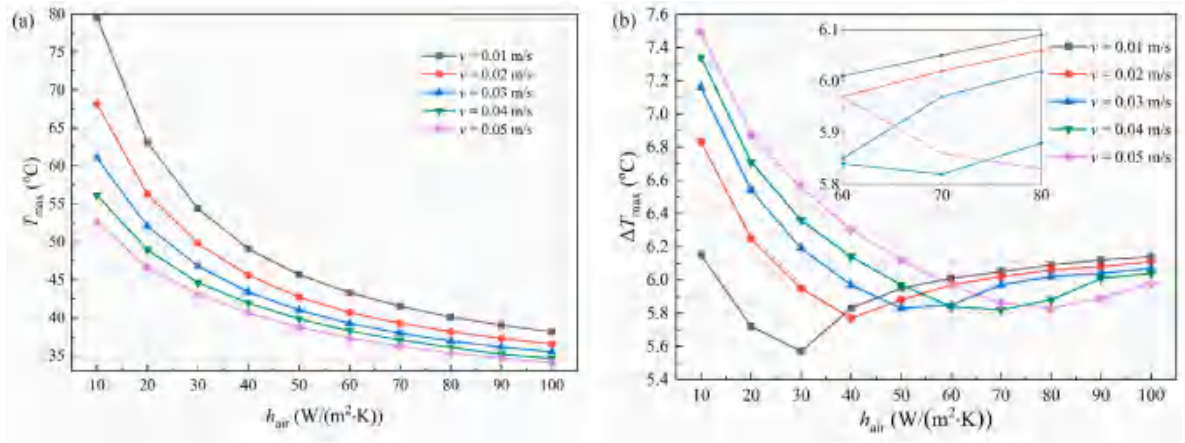

Fig. 10. Effect of air convective heat transfer coefficient on the BTMS thermal performance under different coolant flow rates. (a) T_{max}; (b) ΔT_{max}.

the TEC input current is fixed at 1.5 A. With an increase in the convective heat transfer coefficient, the maximum temperature gradually decreases, as illustrated in Fig. 10(a). When the coolant flow rate is 0.04 m/s, the maximum temperature decreases by 21.55°C as the convective heat transfer coefficient increases from 10 to 100 W/(m^2·K). Moreover, the trend of temperature decrease becomes less pronounced as the air convective heat transfer coefficient increases, and a similar trend is observed for the coolant flow rate. According to Fig. 10(b), when the convective heat transfer coefficient is relatively low, the heat on the hot side of the TEC cannot be effectively dissipated, resulting in poor cooling performance of the TEC. Therefore, the temperature at the bottom of the battery is lower than that at the top. However, as the h_{air} further increases, the cooling performance of the TEC improves and surpasses water cooling, causing the temperature at the top of the battery to become lower than that at the bottom, and the temperature difference begins to increase when $h_{air} > 60$ W/(m^2·K). Meanwhile, considering that the system energy consumption is relatively high at $h_{air} = 60$ W/(m^2·K), and the air convective heat transfer coefficient of 50 W/(m^2·K) already meets the requirements. The heat transfer coefficient is suggested to be 50 W/(m^2·K).

Furthermore, by examining the curves at various coolant flow rates, it becomes evident that although the maximum temperature reduces notably with higher flow rates, the temperature difference actually amplifies. When h_{air} is fixed at 50 W/(m^2·K), the maximum temperature exceeds the limit of 40°C when the coolant flow rate ranges from 0.01 m/s to 0.03 m/s. Therefore, it is necessary to choose a suitable value within the range of 0.04 m/s to 0.05 m/s to balance the maximum temperature and temperature difference.

3.4. Coupling influences of coolant flow rate and TEC input current

This section delves into the examination of how the coolant flow rate influences the thermal performance of the BTMS under different TEC input currents. The objective is to identify the optimal coolant flow rate, as depicted in Fig. 11. Here, the air convective heat transfer coefficient is fixed at the optimal value of 50 W/(m^2·K). The changing trend of maximum temperature and temperature difference with coolant flow rate has been discussed in Fig. 11. In practical applications, the TEC input current varies depending on the temperature working environment, and it is necessary to choose a reasonable coolant flow rate considering the change of TEC current inputs. Clearly, at a current of 1.5 A, the maximum temperature can be maintained below 40°C and the temperature difference remains at a relatively low value. A small TEC input current results in low cooling power of TECs, while an excessive current causes TECs to transform from a cooler to a heater due to the rapid rise in Joule heat. Fig. 11(a) illustrates that the maximum temperature diminishes with an escalation in flow rate; nevertheless, this reduction becomes less prominent once the flow rate exceeds 0.04 m/s. According to Fig. 11(b), it appears that excessive flow rates will cause an increase in temperature difference, accompanied by higher pumping power losses, whereas in the range of 0.02 m/s-0.04 m/s, the temperature difference remains relatively low. Considering that the maximum temperature at 0.04 m/s is apparently lower than those at 0.02 m/s and 0.03 m/s, it is recommended to set the flow rate as 0.04 m/s. Irrespective of variations in TEC input current, both the maximum temperature and temperature difference remain within an acceptable range at this specific flow rate.

3.5. Coupling influences of TEC input current and air convective heat transfer coefficient

Under the optimal coolant flow rate of 0.04 m/s, the influence of TEC input current on the BTMS thermal performance is further analyzed herein, as shown in Fig. 12. According to Fig. 12(a), it is evident that the curves corresponding to different convective heat transfer coefficients exhibit different trends with varying current. When h_{air} is lower than 30 W/(m^2·K), the maximum temperature continuously rises. This is because, in this situation, there is a large temperature difference between the two ends of the TEC, leading to its poor cooling performance. However, when h_{air} is larger than 50 W/(m^2·K), the heat at the hot end of the TEC is effectively dissipated, resulting in a lower temperature difference between the two ends and generating higher cooling power. This causes the maximum temperature to initially decrease and then increase with an increase in current. Although the maximum temperature at $h_{air} = 90$ W/(m^2·K) and 70 W/(m^2·K) is lower than that at 50 W/(m^2·K), it is subject to a higher energy consumption, especially when $h_{air} = 90$ W/(m^2·K), at a current of 1.5 A, the temperature difference is actually higher than that at $h_{air} = 50$ W/(m^2·K), as shown in Fig. 12(b). For the curve of $h_{air} = 50$ W/(m^2·K), the temperature difference gradually decreases with the increase of current from 1 A to 2 A, because the cooling performance of the TEC approaches that of water cooling; If the current is further increased, the cooling performance of the TEC surpasses that of water cooling, leading to an increase in the temperature difference. These phenomena contribute to the corresponding variations in the temperature difference shown in Fig. 12(b). The above results further demonstrate that the convective heat transfer coefficient of 50 W/(m^2·K) is acceptable.

3.6. Effect of the VC thermal conductivity

In the reported literature (Chen et al., 2021; Jang et al., 2022), the equivalent thermal conductivity of VCs ranges from 237 to 20000 W/(m·K), and the equivalent thermal conductivity of 2000 W/(m·K) used in this work refers to (Chen et al., 2021). Under the given optimal

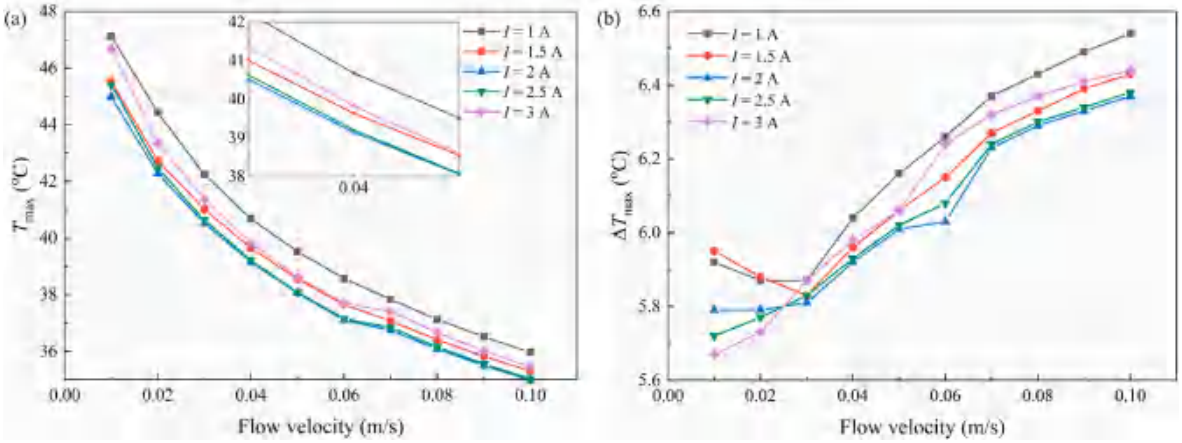

Fig. 11. Effect of coolant flow rate on the BTMS thermal performance under different TEC input currents. (a) T_{max}; (b) ΔT_{max}.

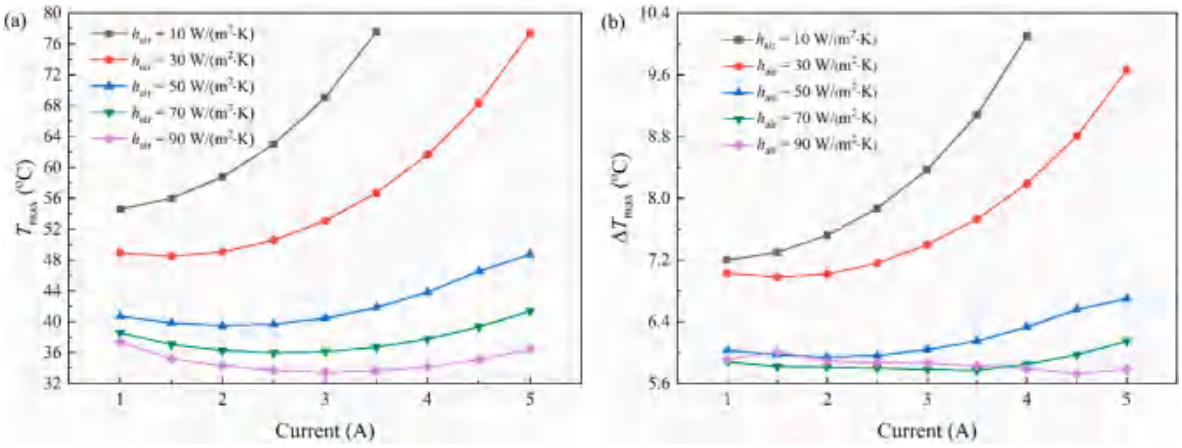

Fig. 12. Effect of TEC input current on the BTMS thermal performance under different air convective heat transfer coefficients. (a) T_{max}; (b) ΔT_{max}.

air convective heat transfer coefficient and coolant flow rate, the effect of the VC thermal conductivity on the maximum temperature and temperature difference of the BTMS is studied, as shown in Fig. 13. The increase in VC thermal conductivity has an insignificant influence on reducing the maximum temperature. This is attributed to the fact that the existing thermal conductivity of 1000 W/(m·K) is already adequate for proficient heat transfer between the batteries and cooling sources. However, the temperature difference is greatly reduced with the increase in the VC thermal conductivity, as illustrated in Fig. 13(b). For the maximum temperature difference limitation of 6°C, the VC thermal conductivity should be larger than 2000 W/(m·K) at least. However, increasing the VC thermal conductivity requires complex structural design and high cost. Therefore, more attention should be devoted to optimizing the cooling devices to improve the thermal performance of the BTMS. A comprehensive structural optimization for this system will be conducted in our future work.

4. Conclusions

In this paper, a new BTMS combined with thermoelectric coolers and vapor chambers is proposed to ensure the optimal working temperatures of batteries. Besides, a complete fluid-thermal-electric multiphysics numerical model is formulated to analyze the thermal characteristics of the BTMS. This model takes into account the interrelationship and coupling effects between thermal, electric, and fluid fields. Taking maximum temperature and temperature difference of batteries as indexes, the effect of different parameters on the thermal performance of the BTMS is comprehensively analyzed through numerical simulations, including air convective heat transfer coefficient, coolant flow rate, TEC input current, and VC thermal conductivity. The results can be briefly summarized as follows:

(1) The fluid-thermal-electric multiphysics numerical model offers an effective method to obtain the overall temperature distributions of the BTMS. According to the numerical results, the use of TECs helps in reducing the battery temperature. However, the temperature difference on both ends of the TEC will deteriorate its cooling performance, and as the input current increases, the cooling power and COP of the TEC exhibit a trend of initial increase followed by a decrease.

(2) Compared with the BTMS without TECs, the integration of TECs into the BTMS results in a noteworthy reduction in the maximum temperature and temperature difference of batteries. Moreover, compared with the BTMS without VCs, the system using VCs can significantly lower the temperature difference. In addition, it is necessary to make a tradeoff between air cooling, water cooling, and TEC input current to ensure good thermal performance and low energy consumption of the BTMS.

(3) Different cooling parameters interact with each other. Although the maximum temperature decreases with the increase of air convection heat transfer coefficient and coolant flow rate, the temperature difference increases at the same time. With the optimal air and water cooling parameters, an increase in the TEC input current leads to an initial decrease and subsequent increase in the maximum temperature and temperature difference. Also, the VC thermal conductivity has little effect on the maximum

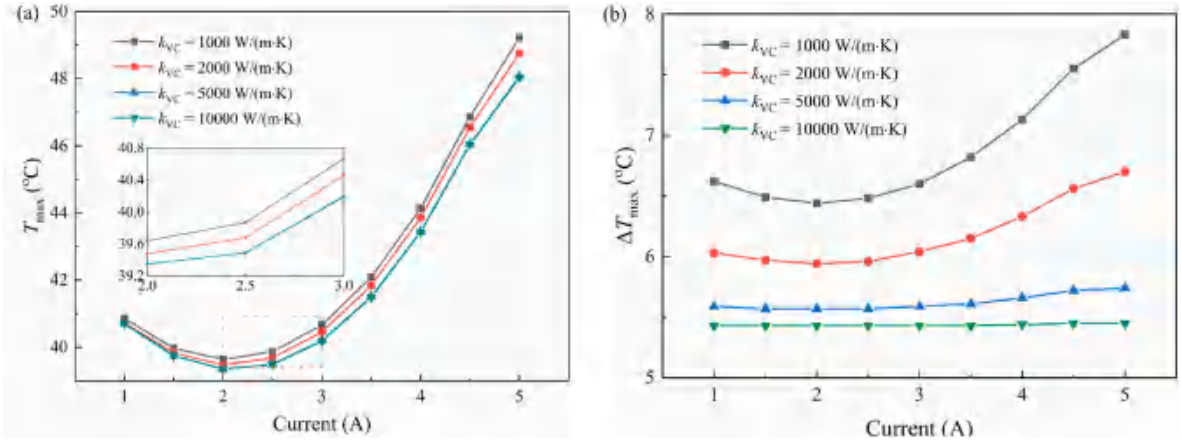

Fig. 13. Effect of the VC thermal conductivity on the BTMS thermal performance. (a) T_{max}; (b) ΔT_{max}.

temperature, but has a significant impact on the temperature difference.

(4) Through analysis, the optimal air convective heat transfer coefficient, coolant flow rate, and TEC input current of 50 W/(m^2·K), 0.04 m/s, and 1.5 A, respectively, are suggested. Under these conditions, the maximum temperature and temperature difference of the battery are 39.83°C and 5.97°C respectively. In practical applications, it should be noted that the mentioned parameters are used for the battery at the ultrahigh discharge rate of 5C. If the battery operates at a lower discharge rate, the corresponding cooling power input can be decreased but should be adjusted simultaneously.

(5) Considering the requirement for a high air convective heat transfer coefficient, optimizations for the finned heat sink and other cooling devices will be conducted in our future work. Also, a comprehensive analysis of the system's energy consumption and application potential will be carried out.

CRediT authorship contribution statement

Ding Luo: Conceptualization, Methodology, Writing – original draft. **Haifeng Wu:** Data curation, Validation, Visualization, Writing – original draft. **Jin Cao:** Formal analysis. **Yuying Yan:** Writing – review & editing. **Xuelin Yang:** Resources. **Bingyang Cao:** Project administration, Supervision, Writing – review & editing.

Declaration of competing interest

We declare that we do not have any commercial or associative interest that represents a conflict of interest in connection with the work submitted.

Data availability

Data will be made available on request.

Acknowledgments

This work was supported by the National Natural Science Foundation of China (Grant Nos. 52306017, U20A20301, 52250273), and the Natural Science Foundation of Hubei Province (No. 2023AFB093).

References

Abbas, S., Ramadan, Z., Park, C.W., 2021. Thermal performance analysis of compact-type simulative battery module with paraffin as phase-change material and flat plate heat pipe. Int. J. Heat Mass Tran. 173, 121269.

Abdulrasool Hasan, H., Togun, H., M Abed, A., I Mohammed, H., Biswas, N., 2023. A novel air-cooled Li-ion battery (LIB) array thermal management system – a numerical analysis. Int. J. Therm. Sci. 190, 108327.

Chen, K., Hou, J., Song, M., Wang, S., Wu, W., Zhang, Y., 2021. Design of battery thermal management system based on phase change material and heat pipe. Appl. Therm. Eng. 188, 116665.

Deng, T., Zhang, G., Ran, Y., 2018. Study on thermal management of rectangular Li-ion battery with serpentine-channel cold plate. Int. J. Heat Mass Tran. 125, 143–152.

Greco, A., Cao, D., Jiang, X., Yang, H., 2014. A theoretical and computational study of lithium-ion battery thermal management for electric vehicles using heat pipes. J. Power Sources 257, 344–355.

Hamisi, C.M., Gerutu, G.B., Greyson, K.A., Chombo, P.V., 2022. Thermal behavior of lithium-ion battery under variation of convective heat transfer coefficients, surrounding temperatures, and charging currents. J. Loss Prevent. Proc. 80, 104922.

Heyhat, M.M., Mousavi, S., Siavashi, M., 2020. Battery thermal management with thermal energy storage composites of PCM, metal foam, fin and nanoparticle. J. Energy Storage 28, 101235.

Hu, Q., Luo, D., Guo, J., Qiu, W., Wu, X., Yang, L., Wang, Z., Cui, X., Tang, J., 2023. Broad temperature plateau for high thermoelectric properties of n-type Bi2Te2.7Se0.3 by 3D printing-driven defect engineering. ACS Appl. Mater. Interfaces 15 (1), 1296–1304.

Isfahani, M.S., Gharehghani, A., Saeedipour, S., Rabiei, M., 2023. PCM/metal foam and microchannels hybrid thermal management system for cooling of Li-ion battery. J. Energy Storage 72, 108789.

Jang, D.S., Yun, S., Hong, S.H., Cho, W., Kim, Y., 2022. Performance characteristics of a novel heat pipe-assisted liquid cooling system for the thermal management of lithium-ion batteries. Energy Convers. Manag. 251, 115001.

Jiang, L., Zhang, H., Li, J., Xia, P., 2019. Thermal performance of a cylindrical battery module impregnated with PCM composite based on thermoelectric cooling. Energy 188, 116048.

Jiang, Z.Y., Qu, Z.G., 2019. Lithium–ion battery thermal management using heat pipe and phase change material during discharge–charge cycle: a comprehensive numerical study. Appl. Energy 242, 378–392.

Jouhara, H., Delpech, B., Bennett, R., Chauhan, A., Khordehgah, N., Serey, N., Lester, S. P., 2021. Heat pipe based battery thermal management: evaluating the potential of two novel battery pack integrations. Int. J. Thermofluids 12, 100115.

Liang, G., Li, J., He, J., Tian, J., Chen, X., Chen, L., 2022. Numerical investigation on a unitization-based thermal management for cylindrical lithium-ion batteries. Energy Rep. 8, 4608–4621.

Liao, G., Jiang, K., Zhang, F., E, J., Liu, L., Chen, J., Leng, E., 2021. Thermal performance of battery thermal management system coupled with phase change material and thermoelectric elements. J. Energy Storage 43, 103217.

Liu, X., Zhang, C.-F., Zhou, J.-G., Xiong, X., Wang, Y.-P., 2022. Thermal performance of battery thermal management system using fins to enhance the combination of thermoelectric Cooler and phase change. Material. Appl. Energy 322, 119503.

Liu, Y., Zhang, J., 2020. Self-adapting J-type air-based battery thermal management system via model predictive control. Appl. Energy 263, 114640.

Lu, Z., Yu, X.L., Wei, L.C., Cao, F., Zhang, L.Y., Meng, X.Z., Jin, L.W., 2019. A comprehensive experimental study on temperature-dependent performance of lithium-ion battery. Appl. Therm. Eng. 158, 113800.

Luo, D., Li, Y., Yan, Y., Hu, X., Fan, X.a., Chen, W.-H., Ren, Y., Cao, B., 2023a. Realizing ultrahigh ZT value and efficiency of the Bi2Te3 thermoelectric module by periodic heating. Energy Convers. Manag. 296, 117669.

Luo, D., Yan, Y., Chen, W.-H., Yang, X., Chen, H., Cao, B., Zhao, Y., 2023b. A comprehensive hybrid transient CFD-thermal resistance model for automobile thermoelectric generators. Int. J. Heat Mass Tran. 211, 124203.

Lyu, Y., Siddique, A.R.M., Majid, S.H., Biglarbegian, M., Gadsden, S.A., Mahmud, S., 2019. Electric vehicle battery thermal management system with thermoelectric cooling. Energy Rep. 5, 822–827.

Mali, V., Saxena, R., Kumar, K., Kalam, A., Tripathi, B., 2021. Review on battery thermal management systems for energy-efficient electric vehicles. Renew. Sust. Energ. Rev. 151, 111611.

Meng, J.-H., Wu, H.-C., Gao, D.-Y., Kai, Z., Lu, G., Yan, W.-M., 2021. A novel super-cooling enhancement method for a two-stage thermoelectric cooler using integrated triangular-square current pulses. Energy 217, 119360.

Murali, G., Sravya, G.S.N., Jaya, J., Naga Vamsi, V., 2021. A review on hybrid thermal management of battery packs and it's cooling performance by enhanced PCM. Renew. Sust. Energ. Rev. 150, 111513.

Osmani, K., Alkhedher, M., Ramadan, M., Choi, D.S., Li, L.K.B., Doranehgard, M.H., Olabi, A.-G., 2023. Recent progress in the thermal management of lithium-ion batteries. J. Clean. Prod. 389, 136024.

Ren, R., Zhao, Y., Diao, Y., Liang, L., Jing, H., 2021. Active air cooling thermal management system based on U-shaped micro heat pipe array for lithium-ion battery. J. Power Sources 507, 230314.

Shahid, S., Agelin-Chaab, M., 2022. A review of thermal runaway prevention and mitigation strategies for lithium-ion batteries. Energy Convers. Manag. X 16, 100310.

Sharma, D.K., Prabhakar, A., 2021. A review on air cooled and air centric hybrid thermal management techniques for Li-ion battery packs in electric vehicles. J. Energy Storage 41, 102885.

Verma, A., Saikia, T., Saikia, P., Rakshit, D., Ugalde-Loo, C.E., 2023. Thermal performance analysis and experimental verification of lithium-ion batteries for electric vehicle applications through optimized inclined mini-channels. Appl. Energy 335, 120743.

Wazeer, A., Das, A., Abeykoon, C., Sinha, A., Karmakar, A., 2022. Phase change materials for battery thermal management of electric and hybrid vehicles: a review. Energy Nexus 7, 100131.

Weragoda, D.M., Tian, G., Burkitbayev, A., Lo, K.-H., Zhang, T., 2023. A comprehensive review on heat pipe based battery thermal management systems. Appl. Therm. Eng. 224, 120070.

Yi, F., E, J., Zhang, B., Zuo, H., Wei, K., Chen, J., Zhu, H., Zhu, H., Deng, Y., 2022. Effects analysis on heat dissipation characteristics of lithium-ion battery thermal management system under the synergism of phase change material and liquid cooling method. Renew. Energy 181, 472–489.

Yue, Q.L., He, C.X., Wu, M.C., Xu, J.B., Zhao, T.S., 2022. Pack-level modeling of a liquid cooling system for power batteries in electric vehicles. Int. J. Heat Mass Tran. 192, 122946.

Zhao, D., Tan, G., 2014. Experimental evaluation of a prototype thermoelectric system integrated with PCM (phase change material) for space cooling. Energy 68, 658–666.

Zheng, M., Liu, Y., Ma, Z., Li, Y., Li, D., Lu, Z., Song, H., Guo, X., Shao, W., 2023. Numerical study on power battery thermal management system based on heat pipe technology. Energy Rep. 9, 350–361.